The Astrophysical Journal, 613:933–947, 2004 October 1

XMM-NEWTON OBSERVATIONS OF NGC 507: SUPERSOLAR METAL ABUNDANCES IN THE HOT INTERSTELLAR MEDIUM

Dong-Woo Kim and Giuseppina Fabbiano
Smithsonian Astrophysical Observatory, 60 Garden Street, Cambridge, MA 02138
Received 2004 March 3; accepted 2004 June 1

ABSTRACT

We present the results of the X-ray *XMM-Newton* observations of NGC 507, a dominant elliptical galaxy in a small group of galaxies, and report supersolar metal abundances of both Fe and α-elements in the hot interstellar medium (ISM) of this galaxy. These results are robust in that we considered all possible systematic effects in our analysis. We find $Z_{\rm Fe} = 2$–3 times solar inside the D_{25} ellipse of NGC 507. This is the *highest* $Z_{\rm Fe}$ reported so far for the hot halo of an elliptical galaxy; this high iron abundance is fully consistent with the predictions of stellar evolution models, which include the yield of both Type II and Type Ia supernovae (SNe). Our analysis shows that abundance measurements are critically dependent on the selection of the proper emission model. The spatially resolved, high-quality *XMM-Newton* spectra provide enough statistics to formally require at least three emission components in each of four circumnuclear concentric shells (within 5′ or 100 kpc): two soft thermal components indicating a range of temperatures in the hot ISM plus a harder component, consistent with the integrated output of low-mass X-ray binaries (LMXBs) in NGC 507. The two-component (thermal+LMXB) model customarily used in past studies yields a much lower $Z_{\rm Fe}$, consistent with previous reports of subsolar metal abundances. This model, however, gives a significantly worse fit to the data (F-test probability < 0.0001). The abundance of α-elements (most accurately determined by Si) is also found to be supersolar. The α-element–to–Fe abundance ratio is close to the solar ratio, suggesting that $\sim$70% of the iron mass in the hot ISM originated from Type Ia SNe. The α-element–to–Fe abundance ratio remains constant out to at least 100 kpc, indicating that Types II and Ia SN ejecta are well mixed on a scale much larger than the extent of the stellar body.

Subject headings: galaxies: abundances — galaxies: individual (NGC 507) — galaxies: ISM — X-rays: galaxies

Online material: color figures

1. INTRODUCTION

Heavy elements in the hot halos of early-type galaxies are the relic of stellar evolution. Determining their abundance is key to our understanding of these galaxies. In particular, since abundances are related to the supernova (SN) yield, they can constrain both the SN rate (Types Ia and II) and the initial mass function (IMF) of the stellar population (e.g., Renzini et al. 1993). Moreover, these measurements are also important for constraining the evolution of the hot interstellar medium (ISM) in terms of the energy input from SNe, which may result in the onset of galactic winds. Yet these measurements are difficult, and the results have been controversial (see Fabbiano 1995).

Fits of *ROSAT* and *ASCA* data with single-temperature thermal spectra (and an additional hard component to account for low-mass X-ray binaries [LMXBs]) suggested a hot ISM almost totally devoid of metals (mostly Fe) in early-type galaxies (e.g., Awaki et al. 1994; Loewenstein et al. 1994; Davis & White 1996). These results are incompatible with the few times solar Fe abundances predicted by stellar evolution models (e.g., Arimoto et al. 1997). Fitting the X-ray spectra with more complex emission models allowed a higher metal content (e.g., Trinchieri et al. 1994; Kim et al. 1996; Buote & Fabian 1998; Matsushita et al. 2000), but complex models were often not statistically required. While Kim et al. (1996) were the first to be able to reject on statistical grounds a simple model in the case of the *ASCA* data of NC 4382, an X-ray faint S0 galaxy, they still could not constrain $Z_{\rm Fe}$ because of the limited statistics of these data.

Higher quality *Chandra* and *XMM-Newton* data are now showing that the extremely low, subsolar iron abundances suggested by the *ROSAT* and *ASCA* analyses can be statistically rejected. In particular, Kim & Fabbiano (2003), by subtracting a population of $\sim$80 discrete sources from the image, excluded subsolar metal abundances in the hot ISM of NGC 1316. Applying a two-temperature model of the hot gas to *XMM-Newton* spectra, Buote (2002) reported the first convincing measurement of supersolar metal abundances ($Z_{\rm Fe} = 1.5$–2 times solar) in the central region of NGC 1399. Central iron abundances that are slightly higher than (or close to) the solar value have been reported for the Virgo cD galaxy, M87 (Gastaldello & Molendi 2002), and nearby galaxy groups, NGC 5044 (Buote et al. 2003) and MKW 4 (O'Sullivan et al. 2003). However, the measured abundances are still not as high as the model predictions, approximately a few times solar. Furthermore, there are still some very low abundance reports: for example, O'Sullivan & Ponman (2004) report $Z < 0.1$ times solar in three X-ray–faint early-type galaxies.

To constrain the heavy-element abundance with good quality data of very high statistical significance, we have performed a deep *XMM-Newton* observation of NGC 507, one of the X-ray brightest early-type galaxies in the *Einstein Observatory* galaxy sample ($F_{\rm X} \sim 10^{-11}$ ergs s^{-1} cm^{-2}; Fabbiano et al. 1992). After the *Einstein Observatory* discovery of X-ray emission from it, NGC 507 has been extensively studied in the X-ray with the *ROSAT* PSPC (Kim & Fabbiano 1995, hereafter KF95), *ROSAT* HRI (Paolillo et al. 2003), *ASCA* (Matsumoto et al. 1997), and *Chandra* (Forman et al. 2001; Kraft et al. 2004). The *ROSAT* PSPC observation of NGC 507 revealed a cooler central region, i.e., a positive temperature gradient (KF95), typical of bright X-ray elliptical galaxies or small groups of galaxies

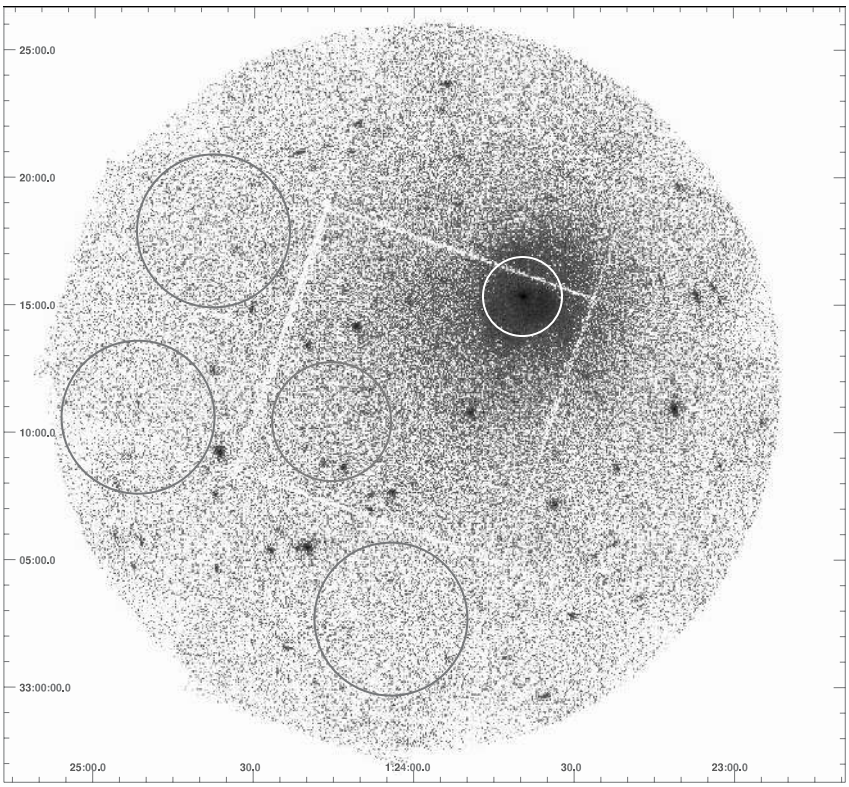

FIG. 1.—*XMM-Newton* (unsmoothed) image. The D_{25} ellipse of NGC 507 is marked with a white ellipse. Also marked are regions from which the three sets of background spectra are extracted. The BL is taken from the circle near the aim point. The second background extraction region is represented by the three large circles near the edge of the field of view. These same regions are also used for scaling the counts from BB data (see text for more details). North is to the top, and east is to the left. [*See the electronic edition of the Journal for a color version of this figure.*]

(e.g., Trinchieri et al. 1997). The values of metal abundances in the hot ISM of NGC 507, reported in the literature, range from 0.2 to near solar (Matsumoto et al. 1997; KF95; Buote & Fabian 1998; Paolillo et al. 2003; Kraft et al. 2004).

This paper is organized as follows: In § 2 we describe the *XMM-Newton* observations and the data reduction. In § 3 we describe the extraction and spectral fitting of the X-ray spectra, considering various effects to assess possible systematic errors; these include background subtraction, emission models, atomic emission codes, deprojection of the data, different ways of grouping heavy elements, and fixing/varying $N_{\rm H}$. In § 4 we present our results on the abundances of Fe and α-elements (Si, S, Mg, and O). In § 5 we discuss the implications of our results in terms of the evolution of the hot ISM and its relation to Types Ia and II SNe. Finally, we summarize our conclusions in § 6.

Through this paper, we adopt a distance $D = 70$ Mpc, based on the heliocentric velocity of 4934 km s^{-1}, or $z = 0.016$ (Huchra et al. 1999), and $H = 70$ km s^{-1} Mpc^{-1}. At the adopted distance, $1'$ corresponds to 20.4 kpc, and the photometric diameter of NGC 507, $D_{25} = 3.'1$, corresponds to 63 kpc.

2. *XMM-NEWTON* OBSERVATIONS

NGC 507 was observed for 40 ks on 2001 January 15, with the *XMM-Newton* MOS and PN (Observation ID [ObsID] 0080540101). We used SAS, version 5.3, to reduce the data and followed the prescriptions in Snowden et al. (2002). We applied flag = 0 for all instruments and, in addition, pattern ≤ 4 for PN to exclude low-quality data. No significant background flare is seen during this observation. The effective exposure time is 34.1 ks for each MOS and 26.6 ks for PN. We also used CIAO, version 3.0, and XSPEC, version 11.2, for further analysis.

Figure 1 shows the *XMM-Newton* (MOS1+MOS2) X-ray image in the broad band (0.3–8 keV). Also marked in Figure 1 are the D_{25} ellipse of NGC 507 and regions where background spectra are extracted (see § 3). The extended X-ray emission from the hot ISM is seen out to $r = 10'$ (this is consistent with previous studies; see KF95; Paolillo et al. 2003). Figure 2 shows the true color image (smoothed with a Gaussian $\sigma = 7.''5$), with red for the soft band in 0.3–0.9 keV, green for the medium band in 0.9–2.5 keV, and blue for the hard band in 2.5–8.0 keV. This image shows that the emission from the central $\sim 1'$ is softer (*yellow*), as suggested by the *ROSAT* PSPC data (KF95). Significant substructures are visible in this central area in the *Chandra* image (Forman et al. 2001; Kraft et al. 2004).

Clearly seen in Figures 1 and 2 are also a large number of apparently pointlike sources at the periphery of the extended hot ISM emission. The number of these sources is in excess of that expected from background serendipitous sources. These sources were first discovered in the *ROSAT* PSPC observations (KF95). We will present the results of point-source properties and spatial analysis of the hot ISM in a future paper. We note here that because these peripheral sources are placed at the *XMM-Newton* aim point, we could obtain reliable background spectra, determined locally at off-axis distances similar to those of the sources (see § 3).

3. SPECTRAL ANALYSIS

We extract spectra for each instrument (MOS1, MOS2, and PN) from several circular annuli using *xmmselect*, available in

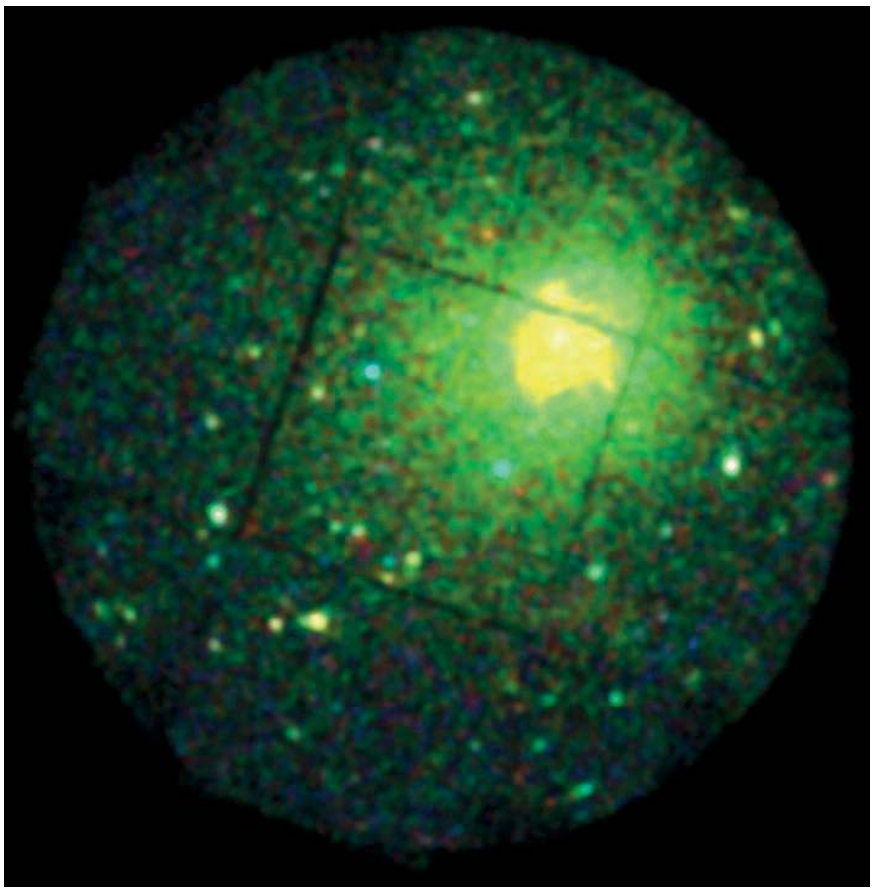

FIG. 2.—*XMM-Newton* true-color X-ray image of NGC 507. MOS1 and MOS2 images are combined and smoothed with a Gaussian with $\sigma = 7\farcs5$. Red represents the soft band (0.3–0.9 keV), green the medium band (0.9–2.5 keV), and blue the hard band (2.5–8.0 keV). North is to the top, and east is to the left.

SAS, version 5.3. The annuli (with the inner to outer radii being $0'$–$1'$, $1'$–$2'$, $2'$–$3'$, $3'$–$5'$, $5'$–$7'$, and $7'$–$10'$) are selected to (1) be at least $1'$ wide, so as to include a few instrumental beam sizes, and (2) yield at least 5000 counts from each individual instrument after background subtraction, to ensure good statistics. Each spectrum extracted from these regions is then binned to have at least 25 counts in order to perform a χ^2 fit. Since we expect very little X-ray emission from the hot ISM (with $kT \sim 1$ or less) at $E > 5$ keV, where instead there is strong background emission, we limit spectral fitting to the energy range of 0.3–5 keV. We note that increasing the upper limit does not improve statistics or change our results. The lower limit is set to avoid the carbon edge at ~0.28 keV and to remove the contamination from the low pulse height events (e.g., Snowden et al. 2002). For each spectral extraction annulus, we determined redistribution matrix files (RMFs) and auxiliary response files (ARFs) with the tools *rmfgen* and *arfgen* available in SAS, version 5.3. Comparing ARFs for different off-axis distances, we find that telescope vignetting is almost independent of energy at $E < 5$ keV. Moreover, the effective areas of different instruments are consistent at $E < 5$ keV but slightly inconsistent at higher energies.

We do not apply any artificial correction factor for different instruments to compensate for systematic cross-calibration uncertainties. Instead, we fit both individual spectra obtained from MOS1, MOS2, and PN and the joint spectra from MOS1+MOS2 and MOS1+MOS2+PN and present all five sets of results to indicate the possible range of parameters. In general, while the best-fit values of the heavy-element abundances may differ, the results are consistent within 90% error (see § 4.2). Best-fit temperatures (and radial variations) are almost identical (see § 4.1). While the goodnesses of fit for all instruments are comparable, PN tends to yield a higher $Z_{\rm Fe}$ than MOS, and a joint fitting of all three instruments gives the average best-fit parameters.

In Table 1, we compare the goodness of the spectral fits performed with various combinations of options. In §§ 3.1–3.4 we discuss in detail the effects of systematic uncertainties on the data extraction and fitting.

The baseline case (fit 1 in Table 1) consists of the five different instrument combinations described above. The observed spectra extracted from the first four annuli ($0'$–$1'$, $1'$–$2'$, $2'$–$3'$, and $3'$–$5'$) are background-subtracted using the local background (BL; see § 3.1) and are fitted simultaneously with projected three-dimensional models (§ 3.3), where each model representing the emission from a three-dimensional shell consists of three spectral components (§ 3.2). The heavy elements are constrained to vary together (§ 3.4), but the overall amounts of elements are fitted independently in each shell. We fix $N_{\rm H}$ at the Galactic value (§ 3.4). The fit is statistically acceptable with $\chi^2_{\rm red}$ close to 1 (always <1.2) with 500–2500 degrees of freedom. Note that χ^2 statistics are determined for the entire set of annuli. Also listed in Table 1 are the best-fit $Z_{\rm Fe}$ and the temperature of the soft thermal component (and their 90% acceptable ranges) in the innermost two regions ($0'$–$1'$ and $1'$–$2'$); these are the key quantities we want to measure in this study (see §§ 4.1 and 4.2). The full range of radial variations of Z and

TABLE 1

GOODNESS OF SPECTRAL FITTING

METHOD	χ^2_{red}	χ^2/dof	Z_{Fe}		kT	
			0′–1′ (0–20 kpc)	1′–2′ (20–41 kpc)	0′–1′ (0–20 kpc)	1′–2′ (20–41 kpc)
Fit 1: Baseline						
BL 3C 3D FNH *Z*1 MOS1	1.05	578/554	2.56 (1.7–3.8)	1.82 (1.2–2.4)	0.85 (0.81–0.89)	0.79 (0.73–0.84)
BL 3C 3D FNH *Z*1 MOS2	1.16	620/535	2.43 (1.5–4.9)	2.24 (1.5–3.3)	0.83 (0.78–0.86)	0.81 (0.75–0.86)
BL 3C 3D FNH *Z*1 MOS12	1.17	1296/1109	2.19 (1.5–3.1)	2.19 (1.6–3.0)	0.84 (0.81–0.87)	0.80 (0.77–0.84)
BL 3C 3D FNH *Z*1 PN	1.21	1731/1428	3.67 (2.3–5.7)	2.32 (1.8–3.1)	0.79 (0.76–0.82)	0.76 (0.71–0.80)
BL 3C 3D FNH *Z*1 MOSPN	1.21	3092/2557	2.85 (2.2–3.8)	2.16 (1.8–2.6)	0.82 (0.79–0.84)	0.78 (0.75–0.80)
Fits 2, 3: Different Background						
BE 3C 3D FNH *Z*1 MOS1	1.37	758/554	1.99	1.61		
BE 3C 3D FNH *Z*1 MOS2	1.83	977/535	1.58	1.58		
BE 3C 3D FNH *Z*1 MOS12	1.68	1862/1109	1.98	1.65		
BE 3C 3D FNH *Z*1 PN	1.53	2184/1428	2.45	2.08		
BE 3C 3D FNH *Z*1 MOSPN	1.67	4269/2557	2.00	1.79		
BB 3C 3D FNH *Z*1 MOS1	1.19	658/554	2.31 (1.7–3.2)	1.81 (1.2–2.8)	0.86 (0.82–0.90)	0.80 (0.72–0.84)
BB 3C 3D FNH *Z*1 MOS2	1.31	703/535	2.22 (1.4–4.9)	2.32 (1.5–4.0)	0.83 (0.79–0.86)	0.82 (0.76–0.86)
BB 3C 3D FNH *Z*1 MOS12	1.29	1430/1109	2.32 (1.7–3.3)	2.08 (1.5–2.7)	0.84 (0.80–0.87)	0.81 (0.78–0.85)
BB 3C 3D FNH *Z*1 PN	1.22	1742/1428	4.08 (3.4–5.4)	2.28 (2.0–2.8)	0.79 (0.76–0.82)	0.76 (0.72–0.80)
BB 3C 3D FNH *Z*1 MOSPN	1.27	3248/2557	3.54 (2.2–4.4)	2.08 (1.8–2.6)	0.81 (0.79–0.84)	0.79 (0.76–0.81)
Fit 4: Different Emission Model						
BL 2C 3D FNH *Z*1 MOS1	1.35	728/539	1.19	1.19		
BL 2C 3D FNH *Z*1 MOS2	1.23	684/558	1.50	0.93		
BL 2C 3D FNH *Z*1 MOS12	1.36	1509/1113	1.33	1.06		
BL 2C 3D FNH *Z*1 PN	1.44	2060/1432	2.34	1.13		
BL 2C 3D FNH *Z*1 MOSPN	1.43	3670/2561	1.43	1.05		
Fit 5: Different Emission Code: APEC						
BL 3C 3D FNH *Z*1 MOS1	0.96	529/554	1.99 (1.4–2.2)	1.61 (1.3–2.3)	0.92 (0.82–1.00)	0.82 (0.79–0.85)
BL 3C 3D FNH *Z*1 MOS2	1.10	588/535	2.12 (1.1–3.9)	2.05 (1.4–3.4)	0.83 (0.80–0.88)	0.84 (0.81–0.93)
BL 3C 3D FNH *Z*1 MOS12	1.10	1217/1109	1.98 (1.5–3.6)	1.76 (1.3–2.2)	0.85 (0.82–0.90)	0.83 (0.81–0.86)
BL 3C 3D FNH *Z*1 PN	1.18	1689/1428	3.53 (2.1–5.8)	1.80 (1.6–2.6)	0.81 (0.78–0.83)	0.82 (0.79–0.84)
BL 3C 3D FNH *Z*1 MOSPN	1.16	2969/2557	2.80 (2.0–4.2)	1.87 (1.6–2.1)	0.82 (0.81–0.84)	0.82 (0.81–0.84)
Fits 6, 7: Without Deprojection						
BL 3C 2D FNH *Z*1 MOS1	1.04	577/554	1.93 (1.6–2.5)	1.34 (1.2–1.7)	0.83 (0.79–0.86)	0.78 (0.71–0.83)
BL 3C 2D FNH *Z*1 MOS2	1.16	619/535	1.94 (1.6–2.3)	1.49 (1.3–1.8)	0.82 (0.79–0.85)	0.80 (0.75–0.85)
BL 3C 2D FNH *Z*1 MOS12	1.17	1293/1109	1.92 (1.6–2.3)	1.45 (1.3–1.7)	0.83 (0.81–0.85)	0.79 (0.76–0.83)
BL 3C 2D FNH *Z*1 PN	1.21	1729/1428	2.32 (2.1–2.7)	1.56 (1.5–1.7)	0.78 (0.76–0.80)	0.74 (0.71–0.78)
BL 3C 2D FNH *Z*1 MOSPN	1.21	3094/2557	2.13 (1.9–2.3)	1.49 (1.5–1.5)	0.80 (0.79–0.82)	0.77 (0.74–0.79)
BL 2C 2D FNH *Z*1 MOS1	1.33	741/558	1.10	0.74		
BL 2C 2D FNH *Z*1 MOS2	1.43	769/539	1.03	0.81		
BL 2C 2D FNH *Z*1 MOS12	1.44	1604/1113	1.06	0.78		
BL 2C 2D FNH *Z*1 PN	1.55	2218/1432	1.12	0.82		
BL 2C 2D FNH *Z*1 MOSPN	1.51	3880/2561	1.09	0.80		
Fit 8: Varying N_H						
BL 3C 3D VNH *Z*1 MOS1	1.03	569/553	2.34 (1.4–3.8)	1.37 (0.9–1.8)		
BL 3C 3D VNH *Z*1 MOS2	1.14	610/534	2.08 (1.4–3.3)	1.37 (1.2–2.1)		
BL 3C 3D VNH *Z*1 MOS12	1.15	1275/1108	1.98 (1.5–2.4)	1.49 (1.2–1.7)		
BL 3C 3D VNH *Z*1 PN	1.19	1690/1427	2.47 (2.3–3.0)	1.51 (1.4–1.7)		
BL 3C 3D VNH *Z*1 MOSPN	1.19	3037/2556	2.03 (1.9–2.4)	1.47 (1.4–1.6)		
Fits 9–12: Varying Different Groups of Elements						
BL 3C 3D FNH *Z*2 MOS1	1.05	578/550	2.87 (1.8–3.7)	1.75 (1.4–2.4)		
BL 3C 3D FNH *Z*2 MOS2	1.17	619/531	2.39 (1.6–4.4)	2.20 (1.5–4.6)		
BL 3C 3D FNH *Z*2 MOS12	1.17	1294/1105	2.29 (1.6–3.5)	2.05 (1.5–2.8)		
BL 3C 3D FNH *Z*2 PN	1.20	1712/1424	3.67 (3.3–4.8)	2.41 (2.1–2.8)		
BL 3C 3D FNH *Z*2 MOSPN	1.21	3085/2553	3.23 (2.1–4.2)	2.16 (1.8–2.7)		

TABLE 1—*Continued*

Method	χ^2_{red}	χ^2/dof	Z_{Fe} 0′–1′ (0–20 kpc)	Z_{Fe} 1′–2′ (20–41 kpc)	kT 0′–1′ (0–20 kpc)	kT 1′–2′ (20–41 kpc)
BL 3C 3D FNH *Z*3 MOS1	1.04	570/550	2.19 (1.6–4.2)	1.68 (1.1–2.6)		
BL 3C 3D FNH *Z*3 MOS2	1.12	596/531	1.76 (1.2–2.5)	1.90 (1.2–3.3)		
BL 3C 3D FNH *Z*3 MOS12	1.15	1267/1105	1.99 (1.5–2.9)	1.97 (1.4–2.4)		
BL 3C 3D FNH *Z*3 PN	1.17	1665/1424	2.69 (1.8–3.5)	2.00 (1.5–2.3)		
BL 3C 3D FNH *Z*3 MOSPN	1.18	3005/2553	2.49 (2.1–3.0)	1.83 (1.6–2.5)		
BL 3C 3D FNH *Z*4 MOS1	0.97	531/546	[3.0]	[2.0]		
BL 3C 3D FNH *Z*4 MOS2	1.05	550/527	[3.0]	[2.0]		
BL 3C 3D FNH *Z*4 MOS12	1.08	1192/1101	[3.0]	[2.0]		
BL 3C 3D FNH *Z*4 PN	1.17	1656/1420	[3.0]	[2.0]		
BL 3C 3D FNH *Z*4 MOSPN	1.15	2930/2549	[3.0]	[2.0]		
BL 3C 3D FNH *Z*5 MOS1	0.97	521/538	2.14 (1.3–3.7)	1.35 (1.0–2.0)		
BL 3C 3D FNH *Z*5 MOS2	1.04	537/519	1.33 (1.0–1.9)	1.53 (1.1–2.3)		
BL 3C 3D FNH *Z*5 MOS12	1.07	1170/1093	1.55 (1.2–2.2)	1.50 (1.2–1.7)		
BL 3C 3D FNH *Z*5 PN	1.16	1639/1412	2.24 (2.0–2.4)	1.89 (1.5–2.5)		
BL 3C 3D FNH *Z*5 MOSPN	1.15	2912/2541	1.91 (1.5–2.2)	1.67 (1.4–2.1)		
Fit 13: Five Shells						
BL 3C 3D FNH *Z*1 MOS1	1.22	881/724	2.83 (1.7–4.3)	1.75 (1.4–3.0)	0.85 (0.82–0.96)	0.80 (0.72–0.85)
BL 3C 3D FNH *Z*1 MOS2	1.24	873/702	2.31 (1.4–5.2)	2.34 (1.6–3.1)	0.83 (0.78–0.87)	0.82 (0.79–0.86)
BL 3C 3D FNH *Z*1 MOS12	1.28	1852/1451	2.04 (1.7–3.7)	2.18 (1.6–3.0)	0.85 (0.83–0.87)	0.81 (0.79–0.84)
BL 3C 3D FNH *Z*1 PN	1.22	2249/1846	4.42 (2.5–9.5)	2.30 (1.8–3.2)	0.79 (0.76–0.82)	0.76 (0.71–0.80)
BL 3C 3D FNH *Z*1 MOSPN	1.27	4220/3322	3.27 (2.3–4.5)	2.08 (1.9–2.7)	0.81 (0.79–0.83)	0.79 (0.76–0.81)
Fit 14: Six Shells						
BL 3C 3D FNH *Z*1 MOS1	1.38	1262/946	2.36 (1.4–4.1)	1.92 (1.5–3.1)	0.86 (0.80–0.90)	0.80 (0.74–0.84)
BL 3C 3D FNH *Z*1 MOS2	1.17	1049/895	2.35 (1.3–3.7)	2.44 (1.7–3.6)	0.82 (0.81–0.87)	0.78 (0.76–0.86)
BL 3C 3D FNH *Z*1 MOS12	1.34	2473/1871	2.68 (1.9–3.9)	1.74 (1.5–2.7)	0.84 (0.80–0.86)	0.82 (0.78–0.85)
BL 3C 3D FNH *Z*1 PN	1.20	2809/2350	4.49 (2.9–7.3)	2.31 (1.9–2.9)	0.79 (0.77–0.83)	0.76 (0.70–0.80)
BL 3C 3D FNH *Z*1 MOSPN	1.29	5439/4221	2.90 (2.3–4.6)	2.15 (1.9–2.7)	0.82 (0.80–0.84)	0.78 (0.76–0.81)

Notes.—The errors in parentheses are at the 90% confidence level. For those methods with poor spectral fitting ($\chi^2_{red} > 1.3$), errors are not meaningful and not listed, except for fits 3, 13, and 14 for comparison (see § 3.3). The quantity kT is the temperature of the soft thermal component. In the "method" column, the following codes are used: For background spectra: (BL) background spectra are taken from the local region (see Fig. 2); (BE) background spectra are taken from the edge of the field of view (see Fig. 2), then scaled by ARFs; (BB) background spectra are taken from the blank field, then scaled by counts in the BL region. For emission models: (2C) two-component model, one soft thermal (VMEKAL) and one hard (7 keV bremsstrahlung); (3C) three-component model, two soft thermal (VMEKAL+1.4 keV VMEKAL) and one hard (7 keV bremsstrahlung). For projection: (2D) no deprojection; (3D) projection of three-dimensional models and comparison with data. For N_H: (FNH) N_H is fixed at the Galactic value (5×10^{20} cm^{-2}); (VNH) N_H is free to vary. For grouping elements: (*Z*1) all heavy elements vary together; (*Z*2) Si and S vary together, and the other elements vary with Fe; (*Z*3) elements lighter than Ca vary with Si, and the rest of the elements vary with Fe; (*Z*4) Fe and Si are fixed, S, Mg, and O vary independently, and the rest of the elements vary as in *Z*3; (*Z*5) Fe, Si, S, Mg, and O vary independently, and the rest of the elements vary as in *Z*3. For the instrument: (MOS1, MOS2, and PN) fitted individually; (MOS12) fitted jointly for MOS1+MOS2; (MOSPN) fitted jointly for MOS1+MOS2+PN.

kT are listed in Table 2. Throughout this paper, we quote errors determined at 90% confidence.

The remaining results (fits 2–14 in Table 1) are obtained by adopting different data extraction or model fitting assumptions. These include (1) using three different sets of background spectra (from the same observations or from blank-field data), (2) using different emission models (two-component and three-component), (3) using different plasma emission codes (MEKAL and APEC), (4) modeling with and without deprojection (two-dimensional and three-dimensional), (5) modeling with N_H fixed at the Galactic value or free to vary, (6) using different ways of grouping elements to vary together (*Z*1–*Z*5), and (7) using the data from the fifth (5′–7′) and sixth (7′–10′) annuli, where the background subtraction is more uncertain (see § 3.3). We note that if not treated correctly, systematic errors could be larger than statistical errors. We discuss each of them in detail.

For the solar abundance, we adopt the element ratios in Grevesse & Sauval (1998). The new meteoric value for Fe is lower (by a factor of 1.48) than the commonly used value in Anders & Grevesse (1989). This change makes Z_{Fe} effectively increase by 50% from those values previously determined (e.g., KF95), even with no other change.

3.1. *Background Spectra*

For extended sources, the accurate determination of the field background counts is often a nontrivial task. To determine the effect of the uncertainties in the choice of field background, we have extracted three different sets of background spectra for each instrument. The first set ("BL" in Table 1) is extracted from a circular region close to the aim point but 7′–12′ away from the center of NGC 507 (discrete sources are excluded). In Figure 1 the circle near the center of the field of view indicates the region of the BL. Because this region is at an off-axis distance comparable to that of our source location, we do not apply corrections for telescope vignetting. The second set ("BE" in Table 1) is extracted from the edge of the detector, 10′–19′ away from the center of NGC 507. The three circles located at the left and at the

TABLE 2

RADIAL VARIATIONS OF SPECTRAL PARAMETERS

Parameter	$r = 0'–1'$ (0–20 kpc)	$r = 1'–2'$ (20–41 kpc)	$r = 2'–3'$ (41–61 kpc)	$r = 3'–5'$ (61–102 kpc)	$r = 5'–7'$ (102–143 kpc)	$r = 7'–10'$ (143–204 kpc)
Three-Component Models						
*Z*1, Fit 1						
$T(1)$	0.82 (0.79–0.84)	0.78 (0.75–0.80)	0.71 (0.65–0.78)	0.63 (0.54–0.73)		
$F_X(1)$	5.25 (3.48–6.89)	4.26 (3.47–5.33)	0.83 (0.56–1.10)	0.81 (0.50–0.98)		
$F_X(2)$	6.75 (4.86–8.71)	12.62 (10.57–14.93)	11.03 (9.09–12.12)	13.08 (11.63–14.85)		
$F_X(3)$	0.82 (0.07–1.49)	1.43 (0.83–2.05)	0.91 (...)	2.77 (1.66–3.64)		
Fe	2.85 (2.23–3.79)	2.16 (1.80–2.58)	1.03 (0.92–1.27)	0.71 (0.62–0.82)		
*Z*2, Fit 8						
$T(1)$	0.81 (0.79–0.84)	0.78 (0.74–0.81)	0.71 (0.60–0.81)	0.64 (0.54–0.73)		
$F_X(1)$	5.18 (3.84–7.95)	4.16 (3.31–5.22)	0.79 (0.50–1.08)	0.82 (0.50–1.16)		
$F_X(2)$	6.75 (5.07–9.78)	12.60 (10.41–15.08)	11.01 (8.67–11.99)	12.96 (11.63–14.85)		
$F_X(3)$	0.90 (0.15–1.62)	1.57 (0.92–2.19)	0.97 (...)	2.94 (1.90–3.87)		
Fe	3.23 (2.15–4.21)	2.16 (1.82–2.65)	1.00 (0.91–1.25)	0.72 (0.62–0.83)		
Si	3.30 (2.75–3.83)	1.94 (1.63–2.28)	0.89 (0.70–1.16)	0.70 (0.54–0.86)		
*Z*3, Fit 9						
$T(1)$	0.81 (0.78–0.84)	0.77 (0.72–0.80)	0.71 (0.56–0.82)	0.59 (0.51–0.76)		
$F_X(1)$	4.76 (3.37–6.68)	3.78 (2.93–4.64)	0.72 (0.40–1.03)	0.77 (0.47–1.13)		
$F_X(2)$	7.07 (4.90–9.67)	12.84 (10.17–15.19)	10.90 (8.52–12.21)	12.55 (11.64–15.59)		
$F_X(3)$	1.03 (0.19–1.73)	1.77 (1.05–2.57)	1.21 (...)	3.56 (1.80–4.41)		
Fe	2.49 (1.83–3.53)	1.83 (1.55–2.31)	0.97 (0.86–1.29)	0.77 (0.61–0.84)		
Si	1.90 (1.53–2.62)	1.32 (1.03–1.80)	0.78 (0.60–1.14)	0.65 (0.44–0.77)		
*Z*4, Fit 10						
$T(1)$	0.78 (0.75–0.81)	0.74 (0.71–0.77)	0.71 (0.62–0.76)	0.57 (0.48–0.69)		
$F_X(1)$	4.73 (4.32–5.19)	3.75 (3.37–4.12)	0.72 (0.46–0.99)	0.70 (0.46–1.01)		
$F_X(2)$	7.10 (6.07–7.97)	12.88 (12.05–13.83)	10.99 (10.32–11.53)	12.94 (12.25–13.58)		
$F_X(3)$	1.06 (0.41–1.73)	1.75 (1.07–2.34)	1.09 (?–8.39)	3.06 (2.10–3.93)		
S	2.16 (1.43–2.95)	1.23 (0.84–1.60)	0.76 (0.45–1.07)	0.44 (0.22–0.66)		
Mg	3.10 (2.40–3.85)	1.63 (1.19–1.84)	0.56 (0.15–1.00)	0.59 (0.28–0.90)		
O	1.49 (1.02–1.99)	1.13 (0.83–1.41)	0.75 (0.49–1.06)	0.58 (0.37–0.81)		
*Z*5, Fit 11						
$T(1)$	0.79 (0.76–0.82)	0.74 (0.71–0.78)	0.71 (0.58–0.78)	0.57 (0.50–0.72)		
$F_X(1)$	4.80 (3.35–6.37)	3.68 (3.00–4.66)	0.70 (0.38–1.01)	0.62 (0.40–0.99)		
$F_X(2)$	7.25 (5.33–9.47)	13.09 (10.55–15.31)	10.96 (9.22–13.29)	13.16 (10.50–14.30)		
$F_X(3)$	0.75 (?–1.78)	1.55 (0.74–2.43)	1.16 (?–4.56)	2.85 (1.87–4.26)		
Fe	1.91 (1.46–2.24)	1.66 (1.43–2.06)	1.01 (0.82–1.09)	0.67 (0.60–0.81)		
Si	2.05 (1.59–2.48)	1.55 (1.29–1.94)	0.94 (0.62–1.20)	0.61 (0.47–0.89)		
S	1.23 (0.62–1.67)	0.97 (0.63–1.39)	0.79 (0.40–1.10)	0.41 (0.20–0.71)		
Mg	1.93 (1.35–2.35)	1.25 (0.88–1.76)	0.59 (0.08–1.01)	0.52 (0.24–0.98)		
O	0.68 (0.25–0.94)	0.78 (0.52–1.16)	0.79 (0.29–0.86)	0.51 (0.36–0.97)		

TABLE 2—*Continued*

Parameter	$r = 0'–1'$ (0–20 kpc)	$r = 1'–2'$ (20–41 kpc)	$r = 2'–3'$ (41–61 kpc)	$r = 3'–5'$ (61–102 kpc)	$r = 5'–7'$ (102–143 kpc)	$r = 7'–10'$ (143–204 kpc)
Two-Component Models						
Three Dimensions, Fit 4						
T(1+2)	0.99 (0.97–1.01)	1.03 (1.02–1.04)	1.41 (1.38–1.43)	1.41 (1.38–1.43)		
Two Dimensions, Fit 6						
T(1+2)	1.03 (1.03–1.04)	1.10 (1.09–1.11)	1.37 (1.35–1.39)	1.40 (1.38–1.43)		
Extra Shells						
Five Shells, Fit 13						
T(1)	0.81 (0.79–0.83)	0.79 (0.76–0.81)	0.71 (0.65–0.77)	0.66 (0.53–0.76)	0.71 (0.70–0.73)	
F_X(1)	5.29 (3.70–8.53)	4.55 (3.40–5.36)	1.15 (0.87–1.44)	1.93 (0.93–3.06)	2.46 (2.23–2.70)	
F_X(2)	7.00 (5.14–9.80)	13.37 (10.62–15.14)	12.44 (10.96–13.99)	18.19 (16.29–19.54)	11.99 (11.03–12.93)	
F_X(3)	0.81 (0.52–1.38)	1.25 (0.64–1.91)	0.74 (0.13–1.30)	1.02 (. . .)	1.67 (1.06–2.28)	
Fe	3.27 (2.29–4.45)	2.08 (1.94–2.65)	1.08 (0.94–1.24)	0.71 (0.64–0.81)	0.75 (0.69–0.83)	
Six Shells, Fit 14						
T(1)	0.82 (0.80–0.84)	0.78 (0.76–0.81)	0.71 (0.65–0.76)	0.69 (0.59–0.78)	0.10 (0.49–0.88)	0.71 (0.70–0.74)
F_X(1)	5.32 (3.67–6.97)	4.51 (3.72–5.31)	1.14 (0.83–1.45)	1.85 (1.39–2.34)	2.00 (. . .)	4.35 (3.89–4.89)
F_X(2)	7.01 (5.75–8.52)	13.40 (11.05–14.63)	12.47 (10.02–13.99)	18.37 (16.29–19.86)	12.86 (11.41–14.49)	13.34 (11.75–14.49)
F_X(3)	0.77 (0.14–1.39)	1.27 (0.70–1.93)	0.72 (0.12–1.33)	0.86 (?–4.84)	1.14 (0.29–1.77)	0.00 (. . .)
Fe	2.90 (2.27–4.63)	2.15 (1.88–2.75)	1.07 (0.95–1.24)	0.77 (0.69–0.88)	0.41 (0.34–0.50)	1.11 (0.97–1.27)

NOTES.—Question marks in the error ranges indicate an unknown limit. [T(1)] temperature of the soft thermal component; [F_X(1)] X-ray flux of the soft thermal component in units of 10^{-13} ergs s^{-1} cm^{-2} at 0.3–8 keV; [F_X(2)] X-ray flux of the 1.4 keV thermal component in units of 10^{-13} ergs s^{-1} cm^{-2} at 0.3–8 keV; [F_X(3)] X-ray flux of the 7 keV LMXB component in units of 10^{-13} ergs s^{-1} cm^{-2} at 0.3–8 keV; [T(1+2)] average temperature of the soft+1.4 keV components, determined in a two-component model.

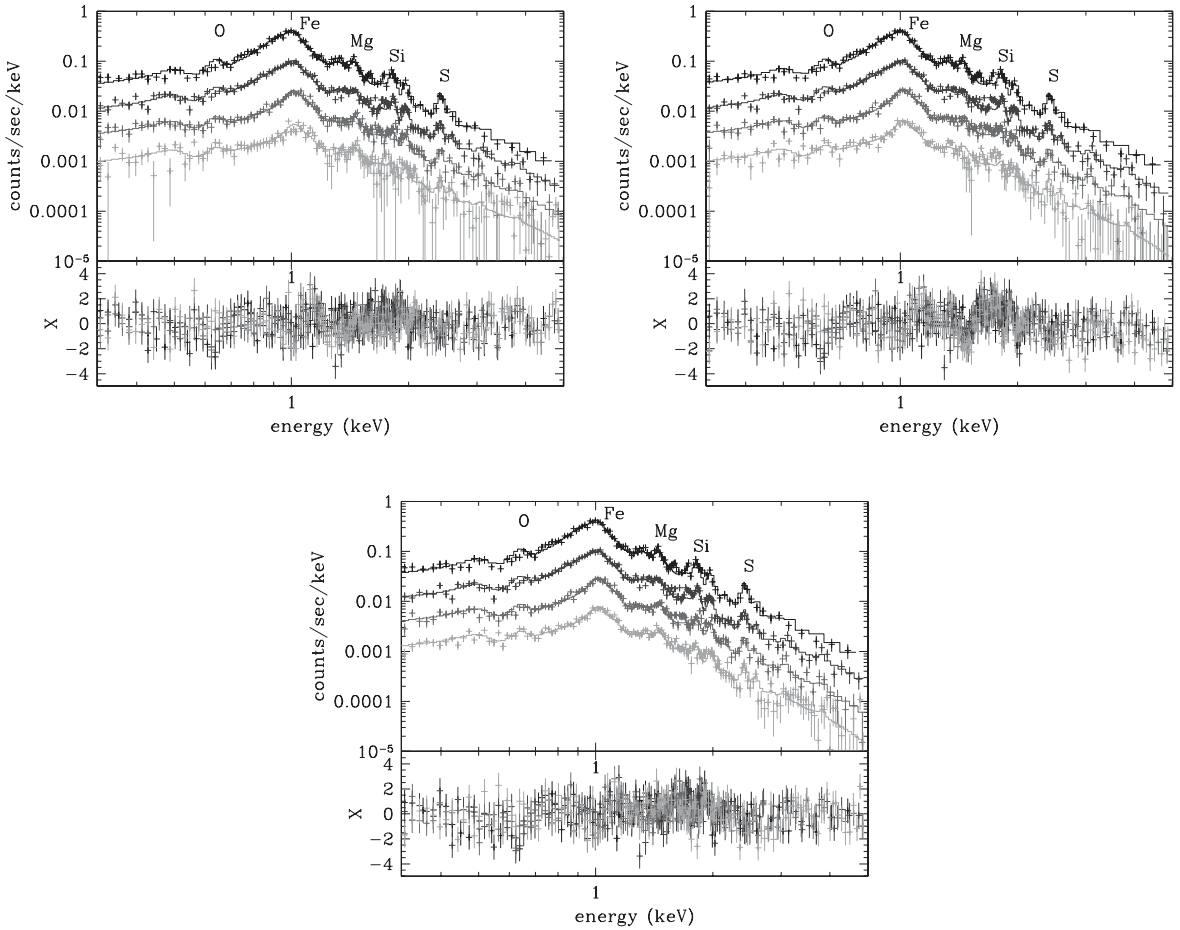

FIG. 3.—Comparison of the results obtained for data extracted with three different sets of background spectra. *Top left*: Source spectra extracted from four concentric annuli and background-subtracted using the BL spectra obtained near the aim point. The data are then fitted together with projected three-dimensional models with three emission components (see text). All the heavy elements vary together (but independently in different shells) and $N_{\rm H}$ is fixed at the Galactic value. Shown are the X-ray spectra extracted from $r < 1'$ and $r = 1'-2'$, $2'-3'$, and $3'-5'$ (*top to bottom*). Except for the first spectrum, they are vertically displaced for visibility. *Top right*: Same as top left but with background spectra taken from the edge of the field of view and rescaled using the ARF at $E < 5$ keV. *Bottom*: Same as top left but with background spectra taken from the BB data and rescaled by the ratio of counts taken from the BL region at $E = 5-10$ keV. [*See the electronic edition of the Journal for a color version of this figure*.]

bottom of Figure 1 indicate the second background region. To these data we apply a vignetting correction based on the effective area ratios given by the ARF at $E < 5$ keV. The third set ("BB " in Table 1) is derived from the blank-field background data obtained from the *XMM-Newton* Science Operations Centre (Lumb et al. 2002). In this case, the background spectra are extracted from the same annuli as the source spectra. Because of the temporal and spatial variation of the background count rate (see Lumb et al. 2002), we rescaled the BB spectra to our data by comparing the counts extracted from the same location (Fig. 2, *red circle*) in the energy range of 5–10 keV.

The results of the spectral fits using the three different background spectra are compared in Figure 3 for the MOS1 data (the results from other instruments are similar). The X-ray spectra (and the best-fit models) extracted from $r < 1'$ and $r = 1'-2'$, $2'-3'$, and $3'-5'$ are shown from top to bottom. Except for the first spectrum, they are vertically displaced for visibility. Strong emission features are also marked. The BL subtraction always gives a significantly better fit than the other two (compare fits 1–3 in Table 1). The spectra obtained with BL subtraction (Fig. 3, *top left*) work well throughout the whole energy range, resulting in $\chi^2_{\rm red}$ close to 1 and no localized deviations near strong emission features. Instead, using background spectra taken at the edge of the field (BE; Fig. 3, *top right*) or from the BB data (Fig. 3, *bottom*) produces poor fits with $\chi^2_{\rm red}$ values of 1.4–1.8 and 1.2–1.3. The *F*-test indicates that the fit of the BL-subtracted spectra results in a significantly improved χ^2 (a probability of <0.0007 and 0.05–0.1 for BE and BB, respectively). The significant deviations at $\sim$1.5 keV (and also at $\sim$2 and $\sim$2.3 keV) seen in BB and BE spectra are likely to stem from incorrect subtraction of the Al K fluorescent emission (Lumb et al. 2002). Also visible at high energies (>4 keV) are oversubtraction (BE) or possibly undersubtraction (BB) features.

Based on this analysis, we chose to rely on the BL estimate, except for the outer source annuli (§ 3.3), where we use BB background because the BL obtained at $r = 7'-12'$ may be contaminated by the X-ray emission of the extended hot ISM (see § 3.3). We note that while the relative fluxes differ, particularly at the outer shell, the abundance and temperature are consistent within the error between BL and BB (compare fits 1 and 3 in Table 1).

3.2. *Emission Models*

The X-ray emission from early-type galaxies can consist of many different emission components: hard X-ray emission

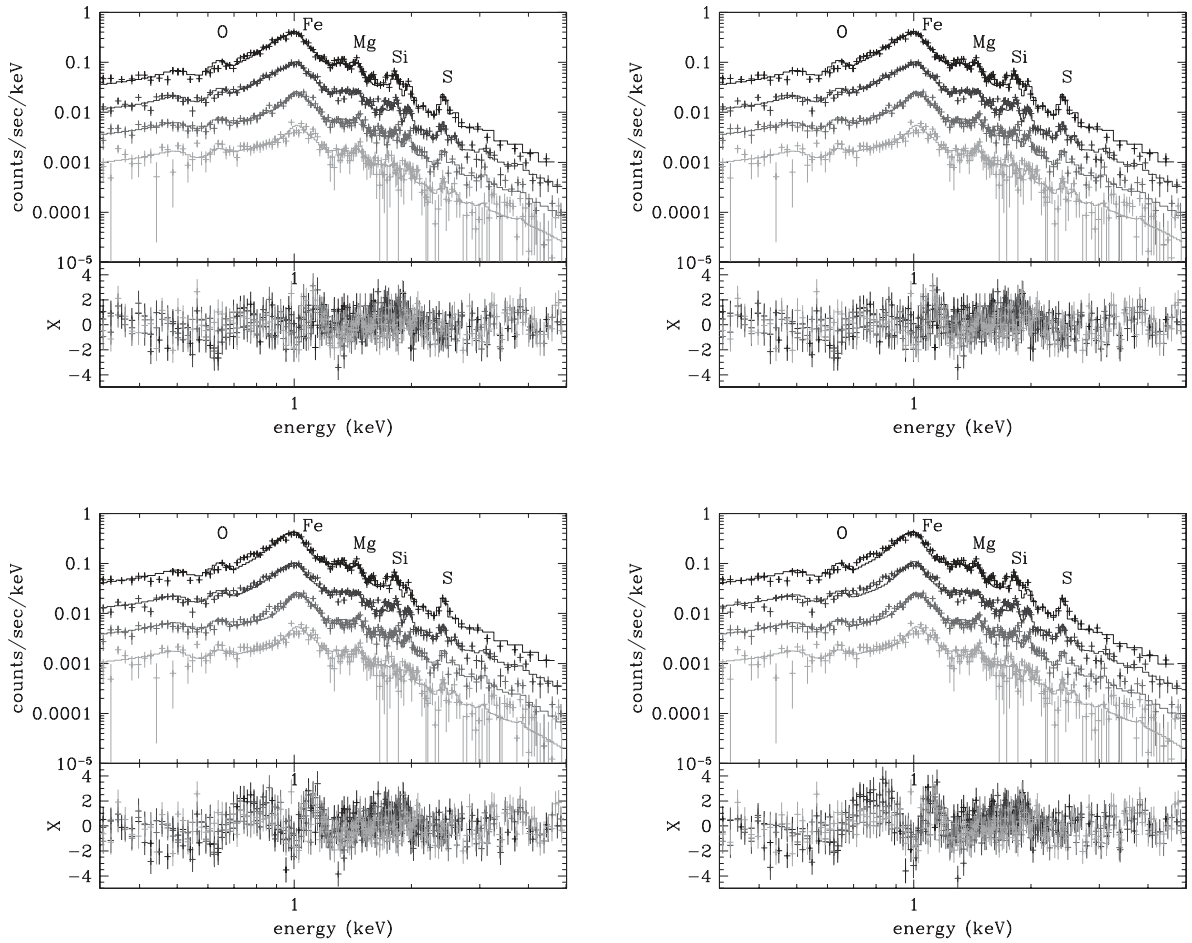

FIG. 4.—Comparison of spectral fitting with three-component vs. two-component models and three dimensions vs. two dimensions. This is the same as Fig. 3 (*top left*) but for three-component models and three-dimensional fitting (*top left*), two-component models and three-dimensional fitting (*top right*), three-component models and two-dimensional fitting (*bottom left*), and two-component models and two-dimensional fitting (*bottom right*). [*See the electronic edition of the Journal for a color version of this figure.*]

from LMXBs, soft thermal emission from the hot ISM, and possibly a power-law component from a low-luminosity active galactic nucleus (AGN), not to mention some additional hard emission from incompletely subtracted background sources. In NGC 507 the nuclear emission is not a major component (this will be discussed in a future paper). The LMXBs are instead likely to contribute substantially to the hard emission, although we do not see them directly because typical LMXB luminosities are below the detection threshold of these observations (see § 5). The hot ISM of early-type galaxies is likely to consist of multitemperature gas. For NGC 507, the *ROSAT* data suggested that the average temperature increases with increasing galactocentric distance (KF95). We cannot exclude multitemperature, possibly inhomogeneous, hot gas (see later in §§ 4.1 and 5). Therefore, at least three emission components (two thermal components to give a measure of the range of temperatures in the hot ISM plus a hard component to model the LMXB emission) are needed to fit the spectra from each annulus. This is a "minimum" component model, and the real emission could be more complex.

We use a Mewe-Kaastra-Liedahl (MEKAL) thermal plasma model for the thermal emission. We let the temperature of the softer thermal component vary and fix that of the harder thermal component at 1.4 keV, which is the average ISM temperature suggested by *ROSAT* data at large galactocentric distances (KF95; see § 4.1). We note that even if the temperature of the harder thermal component is set to vary, it is consistent with being 1.4 keV within the error, and our results (including the measured abundance and soft component parameters) remain almost the same. We have also applied an APEC plasma emission code[1] and listed the results in Table 1 (fit 5). The results are similar to those of the baseline case (fit 1). Because LMXBs appear to exhibit uniform spectral properties, we adopt a $kT = 7$ keV bremsstrahlung component to model their spectrum (e.g., Kim & Fabbiano 2003; Irwin et al. 2003), although the temperature is not critical in our results as long as $kT \gtrsim 3$ keV.

The need for a three-component model is demonstrated by a comparison with two-component fits in Figure 4 (*top left*, *top right*). We find a significant improvement with the three-component model, clearly indicating the presence of thermally complex ISM (also compare fits 1 and 4 in Table 1). *F*-tests for three components over two components indicate very low probabilities of exceeding the given *F*-statistic ($<10^{-4}$). The localized deviation near the Fe peak ($\sim$1 keV) is clearly seen in the two-component fit (Fig. 4, *top right*). This kind of deviation is reminiscent of the results of spectral fits with previous X-ray missions, which resulted in an extremely low Z with a small error (e.g., Matsushita et al. 1994; Matsumoto et al. 1997). We reproduce the same trend that the best-fit $Z_{\rm Fe}$

[1] See http://cxc.harvard.edu/atomdb/sources_apec.html.

in the two-component fit is significantly lower than in the three-component fit (see § 4.2).

It is known that some atomic data may be uncertain, particularly for Fe XVII lines (e.g., Xu et al. 2002). To test the effect of these uncertainties on our results, we have refitted the *XMM-Newton* spectra after (1) excluding the energy ranges (0.7–0.75 and 0.8–0.85 keV) of Fe XVII lines (15.01, 16.78, 17.951, and 17.096 Å) and (2) adjusting the line ratios (increasing by ∼50% the 16.78, 17.951, and 17.096 Å lines) based on Capella data (Canizares et al. 2000). In both tests, our results remain the same. This is because Fe XVII lines are not very strong in NGC 507 because of the ISM temperature being higher than 0.6 keV (0.8–1.4 keV in the center; see Fig. 3, in which the Fe peak is at ∼1 keV, instead of 0.7–0.8 keV) and because the CCD spectra are not sensitive to over- or underestimated individual lines. This is also confirmed by the identical results obtained with different emission codes (MEKAL vs. APEC). Xu et al. (2002) point out that some strong lines (e.g., Fe XVII λ15.01) may be optically thick near the center. We did not correct for resonance scattering in our analysis. However, we expect the resonance scattering will not change our results, as indicated in test 1 above; this effect, if added, will only increase the measured abundance.

3.3. *Deprojection*

Since the ISM is not isothermal, and there is a radial temperature gradient, we need to deproject each spectrum obtained from a two-dimensional annulus, assuming spherical symmetry. To this end we used *project*, available in XSPEC, version 11.2, where three-dimensional models (representing spectra from three-dimensional shells) are projected into a plane and simultaneously fitted to a set of observed spectra extracted from multiple annuli. We compare the results of three-dimensional versus two-dimensional fitting in Figure 4 (*top left*, *bottom left*) (or compare fits 1 and 6 in Table 1, for the three-component model). Similarly, for two-component models, three-dimensional and two-dimensional results are compared in Figure 4 (*top right*, *bottom right*) (or compare fits 4 and 7 in Table 1). Although the difference between three-dimensional and two-dimensional fits is less significant (and the $\chi^2_{\rm red}$ more similar) than that between three-component and two-component models, the two-dimensional fits produce a lower $Z_{\rm Fe}$ than the three-dimensional in all cases. We note that the combination of a two-component model and two-dimensional fitting yields the lowest $Z_{\rm Fe}$: this is the typical approach found in published work (see § 5).

To most accurately determine abundances in the hot ISM, our baseline case (fit 1 in Table 1) used the spectral data up to $r = 5'$ or ∼100 kpc and the BL. As described in § 3.1, the BL provides the best χ^2 statistics. However, the diffuse X-ray emission extending to 10′ (e.g., KF95) may affect our results in the inner region. To quantify the projection effect of the outer region (from 5′ to 10′), we repeat the deprojection by adding the outer two shells of 5′–7′ and 7′–10′ (fits 13 and 14 in Table 1). As the BL may contain emission from the extended sources, we apply the background spectra obtained from the BB data and compare the results with different outer shells with the same background data (i.e., fits 3, 13, and 14 in Table 1). The results in the inner four shells (<100 kpc) are consistent within the errors. In particular, the metal abundances remain unchanged (see also Table 2).

Since there have been reports of central minima ($r < 0.'5$) of metal abundances, e.g., in M87 (Gastaldello & Molendi 2002) and in NGC 5044 (Buote et al. 2003), we have also divided the central bin ($r < 1'$) into two parts ($r < 0.'5$ and $r = 0.'5$–$1'$) to check for small-scale variation in the central region. We do not find any significant difference inside $r < 1'$ of NGC 507 (this is not surprising, given the *XMM-Newton* point-spread function size; Ehle et al. 2003): $Z_{\rm Fe}$ increases slightly toward the center (MOS) or remains constant (PN).

3.4. *Linking Element Abundances*

Given the limited statistics and the various systematic effects (e.g., blending of emission features in the low-resolution CCD spectra and the presence of a strong Al K fluorescent line), it is not always possible, nor optimal, to vary all the heavy elements independently. We have therefore linked different group of elements to vary together. First (*Z*1), all elements vary together with Fe, and their relative abundances are fixed at the solar ratio given by Grevesse & Sauval (1998). Second (*Z*2), Si and S (the two most prominent elements among α-elements) vary together, and the rest of the elements are tied to Fe. Third (*Z*3), elements lighter than Ar are tied to Si, and those heavier than Ca to Fe, to distinguish α-elements and those mostly produced by Type Ia SNe. Fourth (*Z*4), Fe and Si are fixed at the average best-fit values in *Z*1–*Z*3, and S, Mg, and O vary independently, while the other elements are tied as in *Z*3. Fifth (*Z*5), Fe, Si, S, Mg, and O vary independently, and the other elements are tied as in *Z*3. In general, while the goodness of the fit is almost the same regardless of different grouping, the best-fit abundances vary somewhat (see § 4.3).

We tried to independently vary the abundances of two thermal components (in three-component models) to test the abundance inhomogeneity, where the metal-rich gas could cool more rapidly. However, with our statistics, we could not see any significant difference. The accurate abundance measurement of individual components will require a much higher signal-to-noise ratio and higher resolution data.

3.5. $N_{\rm H}$

Finally, we either fix $N_{\rm H}$ to the Galactic value (5×10^{20} cm^{-2}) or let it vary freely (fit 8 in Table 1). The best-fit $N_{\rm H}$ is consistent with the Galactic value at ∼3 σ. We find that $N_{\rm H}$ often goes together with the amount of the hard component and affects $Z_{\rm Fe}$, in the sense that a larger $N_{\rm H}$ and a larger hard component effectively reduce $Z_{\rm Fe}$. We discuss this effect in § 5.

4. RESULTS

4.1. *Temperatures of Multicomponent Emission Models*

Our results are consistent with the overall positive temperature gradient suggested by the *ROSAT* PSPC data (KF95). In addition, we find that the hot ISM within each three-dimensional shell is not isothermal and that a range of *kT* is required. In Table 2 we list the spectral parameters determined in each shell, obtained by jointly fitting the spectra from all the instruments (MOSPN in Table 1). We compare the radial variation of the relative contributions from different emission components in Figure 5. We plot the results of the baseline case (fit 1 in Table 1); note that other three-component models yield similar distributions of temperatures and flux ratios. The temperature of the first soft component (circles in Fig. 5, *left*) ranges from 0.6 to 0.8 keV (see Fig. 5, *left*). The X-ray flux ratio of the two thermal components measures the relative importance of cooler (0.6–0.8 keV; circles in Fig. 5, *right*) and hotter (1.4 keV; open triangle in Fig. 5, *right*) emission. In the innermost shell ($r < 20$ kpc), the contributions from the two components are roughly equal, while in the second shell

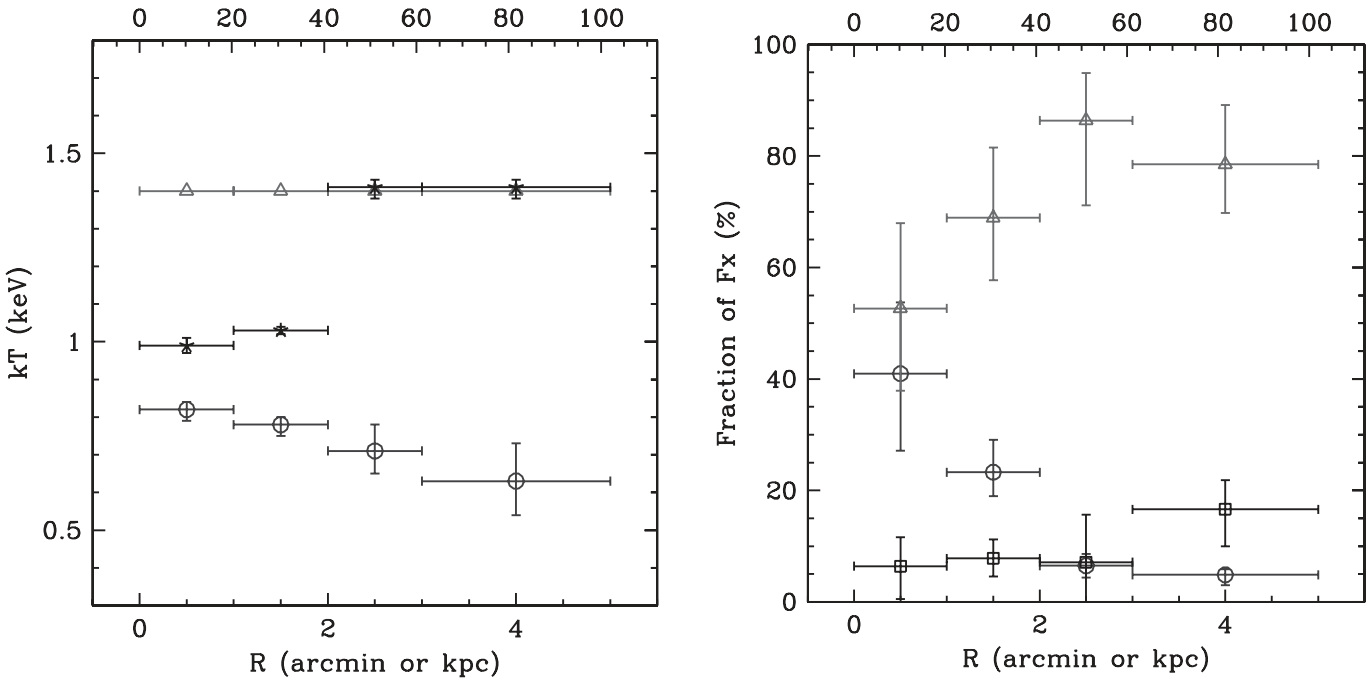

FIG. 5.—*Left*: Radial distribution of temperatures in the hot ISM. The circles and triangles represent the cooler and hotter components in the three-component models, respectively. The asterisks represent emission-averaged temperatures determined with two-component models. *Right*: Radial distribution of the relative fluxes of three emission components. The circles and triangles represent the cooler and hotter thermal components, respectively, while the squares represent the hard LMXB component. [*See the electronic edition of the Journal for a color version of this figure*.]

($r = 20$–40 kpc), there is a smaller amount of cooler component than in the central bin, with a ratio of 1:3. In the outer shells ($r > 40$ kpc), the ratio drops to 1:12, and the gas at $\sim$1.4 keV dominates the X-ray emission. Note that the cooler component is still required in the outer shells, even though it is relatively small.

In Table 2 (at the bottom) and Figure 5 (*left*, *crosses*), we also show the best-fit gas temperatures obtained with two-component models (fits 4 and 7 in Table 1). Although the fits are not acceptable, we can consider the resulting temperatures as the emission-averaged temperatures of the hot ISM. This emission-averaged temperature is $\sim$1 keV near the center and increases to $\sim$1.4 keV at the outskirts, consistent with the measurements in KF95. We also tried cooling flow models (*vmkcflow* in XSPEC). In this case, the low kT is $\sim$0.6 keV, and the high kT is $\sim$1.4 keV near the center, but the fit is poor ($\chi^2_{\rm red} \sim 1.5$). As reported for other early-type galaxies and clusters (Buote et al. 2003; Peterson et al. 2001), we detect no thermal emission from gas with $kT < 0.6$ keV for any choice of emission model.

The third (hard LMXB) component (squares in Fig. 5, *right*) accounts for $\sim$7% of the total X-ray emission in the first two shells (i.e., within the optical galaxy, $r < 40$ kpc), which is consistent with the expected amount from LMXBs (see § 5). Its amount is undetermined (or possibly absent) in the third shell ($r = 40$–60 kpc). Instead, a nonnegligible amount of hard component is required in the fourth shell ($r = 60$–100 kpc). This hard emission may originate from background AGNs or may be due to sources similar to the sources detected at larger distances, in excess of the deep survey background predictions. (This will be further discussed in a future paper.)

In summary, (1) the emission-averaged temperature of the hot ISM increases with increasing distance from the center (from $\sim$1.0 to $\sim$1.4 keV); (2) the hot ISM is not locally isothermal: at least two components are needed to fit the data, with the cooler one ($kT \sim 0.6$–0.8 keV) contributing proportionally more at smaller radii; (3) at least three emission components, including a hard component probably from a population of sources unrelated to the hot ISM, e.g., LMXBs, are required.

4.2. *Iron Abundance*

The radial distribution of the Fe abundance is shown in Figure 6 (*left*) (see also Table 2). The best-fit $Z_{\rm Fe}$ is $\sim$3 times solar in the center ($r < 1'$ or $<$20 kpc), $\sim$2 times solar at $r =$ 20–40 kpc, and similar to (or slightly lower than) solar at $r >$ 40 kpc. The acceptable range of $Z_{\rm Fe}$, given by the statistical error at 90% confidence, is roughly ± 1 solar in fitting the spectra from individual instruments, or $\pm\frac{1}{2}$ solar in the joint fits of the spectra from all the instruments. The maximum $Z_{\rm Fe}$ could be as high as 4 times solar inside the D_{25} ellipse of the galaxy.

The presence of supersolar $Z_{\rm Fe}$ in NGC 507 and its negative radial gradient are robust results, as shown by the comparison of the fits obtained with the different approaches used in this study. Varying $N_{\rm H}$ slightly reduces $Z_{\rm Fe}$ (fit 8; see also § 5). Different methods of grouping the heavy elements (fits 1 and 9–12 in Table 1) result in similar values of $Z_{\rm Fe}$. Fit 12 ($Z5$, in which Fe, Si, S, Mg, and O vary independently) appears to produce the lowest $Z_{\rm Fe}$, but it is still consistent with other results within the acceptable range. In this case, $Z_{\rm Fe}$ in the second shell remains similar to that in the center (i.e., a shallow gradient). The supersolar $Z_{\rm Fe}$ is not affected by the uncertainty in the background spectra. Although the fit with different background spectra (BE and BB) may be poor (see fits 2 and 3), $Z_{\rm Fe}$ still ranges between 2 and 4 times solar in both cases, consistent with the BL. We also note that the Fe abundance measured in the central $2'$ region will be the least affected by background uncertainties. In addition, the uncertainties of the plasma emission codes do not affect our results (see § 3.2). Considering all these various systematic effects, we conclude that $Z_{\rm Fe}$ is 2–3 times solar within the optical confines of NGC 507.

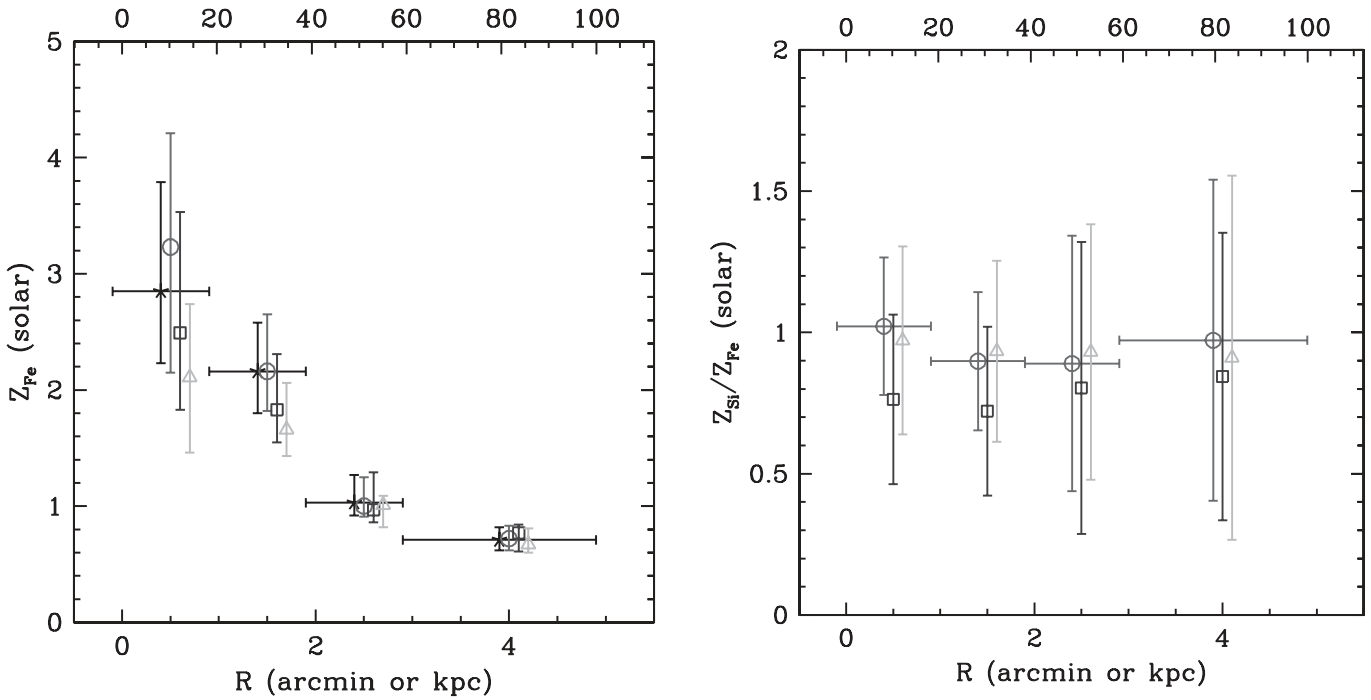

FIG. 6.—*Left*: Radial distribution of Fe abundances The asterisks, circles, squares, and triangles are determined by *Z*1, *Z*2, *Z*3, and *Z*5 (see Table 1). *Right*: Radial distribution of the Si-to-Fe abundance ratio. The circles, squares, and triangles are determined by *Z*2, *Z*3, and *Z*5 (see Table 1). [*See the electronic edition of the Journal for a color version of this figure*.]

We note that the lowest Z_{Fe} value is obtained with the two-component model with two-dimensional fitting (fit 7 in Table 1; Fig. 4, *bottom right*). In this case, the best-fit Z_{Fe} is approximately solar, which would be $\sim$0.6 times solar with Anders & Grevesse (1989) solar ratios, close to the previously reported subsolar abundance (e.g., Matsushita et al. 2000; see also Kraft et al. 2004). The effect of the adoption of a two-component model on the abundance measurement is further discussed in § 5. Recent analysis of *XMM-Newton* RGS data suggested that the metal abundance is subsolar in NGC 4636 (Xu et al. 2002) and NGC 533 (Peterson et al. 2003). Although the RGS data have high spectral resolution, the analysis of slitless spectra is complicated and depends heavily on a considerable amount of Monte Carlo simulations and modeling. Future independent confirmation of these results would be desirable.

4.3. *Abundance Ratios of Different Heavy Elements*

After Fe, Si has the strongest emission features. These lines are relatively isolated around $\sim$2 keV and hence provide the most reliable measurement of α-element abundances. In Table 2 we list the results obtained from different groupings of heavy elements (*Z*2 and *Z*3; see § 3.4). Although these results are slightly method dependent, *Z*2 giving a slightly higher Z_{Si} than *Z*3, they are all consistent at $\sim$2 σ (or better) significance. On average, the best-fit Z_{Si} ranges from 2 to 3 times solar within the D_{25} ellipse and decreases to approximately solar outside the optical galaxy, generally following the behavior of the iron abundance. The ratio of Si to Fe is therefore close to solar in all radial bins, i.e., there is no radial gradient of [Si/Fe] (see Fig. 6, *top right*). The solar ratio of Si to Fe is consistent with previous reports (e.g., Matsushita et al. 2000), although the absolute abundances in these studies (Z_{Fe} or Z_{Si}) are generally lower than those we find here. This ratio is also consistent with the [Si/Fe]-*kT* relationship of galaxies and clusters (e.g., Fukazawa et al. 1998).

Abundance measurements of the other α-elements are not as reliable as those of Si. This is because their emission features are weaker and/or confused, and in some cases (Mg, O) affected by calibration uncertainties. S, Mg, and O are set to vary independently in *Z*4 and *Z*5 (§ 3.4). Although the χ^2_{red} values are almost the same in the two cases (compare fits 11 and 12 in Table 1), the best-fit abundances are higher in *Z*4 than in *Z*5, but the differences are always within the 90% error.

The emission features of S are found next to those of Si around $E \sim 2.5$ keV. They are also relatively isolated, but weaker than those of Si. The best-fit Z_S is slightly lower than Fe or Si. S/Fe is $\sim$0.6 and barely consistent with solar at 90% confidence. No significant radial variation of S/Fe is evident.

The Mg emission features around $E \sim 1.5$ keV can be easily identified in thermal gas emission with $kT < 1$ keV. However, Fe features start to blend with the Mg features in the hotter X-ray plasma with $kT > 1$ keV. Because the hot ISM in NGC 507 has at least two temperatures in the range $kT = 0.6$–1.4 keV (see § 4.1), the Mg features are somewhat mixed with the Fe emission. The Mg abundance is also somewhat uncertain, because also present at $E \sim 1.5$ keV is a strong Al K fluorescent line from the camera body (Lumb et al. 2002). The best-fit Z_{Mg} is slightly lower than Fe or Si. Mg/Fe is $\sim$0.8 but consistent with solar at 90% confidence. As in the case of Si and S, there is no significant radial variation of Mg/Fe.

The emission features of O are at $E \sim 0.6$–0.7 keV (or $\sim$0.5 keV for the colder plasma). They are relatively isolated but partially blended (at $E \sim 0.7$ keV) with the Fe features in plasmas with $kT = 0.5$–1 keV. The best-fit O/Fe is lowest (0.3–0.5 times solar) among the measured α-elements within the D_{25} ellipse, while consistent with solar at larger distances. The significance of deviation from the solar ratio is $\sim$4 σ at $r < 20$ kpc and $\sim$3 σ at $r = 20$–40 kpc. Given that the instrument calibration is least accurate at lower energies and that

absorption may affect the result in this band, we consider the underabundant O as suggestive but not conclusive evidence.

5. DISCUSSION

5.1. *Elemental Abundances and Supernova Yields*

As discussed in § 1, the low, often subsolar abundance of heavy elements, particularly iron, reported in the hot ISM of early-type galaxies has been the subject of controversy (see Fabbiano 1995). Iron, in particular, which exhibits the strongest X-ray emission features, is predicted to have 2–5 times solar abundance in the hot ISM (see Arimoto et al. 1997): the Fe abundance in the hot ISM is expected to be at least similar to (or higher than) that of the stellar population in elliptical galaxies, where iron was initially synthesized by the bulk of Type II SN explosions and then enriched during the lifetime of the galaxy by Type Ia SNe.

While we had in the past suggested that these apparent low metal abundances are the result of hidden complexity of the X-ray spectra (see discussion in Fabbiano 1995; Kim et al. 1996; see also Buote & Fabian 1998), this conclusion was difficult to prove with the data available then. Our *XMM-Newton* spectra of NGC 507 clearly require a departure from a simple locally isothermal emission model for the hot ISM, resulting in a robust determination of supersolar Fe abundances, fully in agreement with the metal enrichment theory (e.g., Arimoto et al. 1997): $Z_{\rm Fe} \sim 2$–3 times solar and possibly up to $\sim$4 times solar at the center of NGC 507. The measured iron abundances indicate a negative radial gradient (Fig. 6, *top left*). Because the stellar density profile is much steeper than the gas density profile (for example, $\rho_* \sim r^{-3}$, while $\rho_{\rm gas} \sim r^{-1.5}$, if $\Sigma_{\rm opt} \sim \Sigma_{\rm X} \sim r^{-2}$), the metal enrichment by mass loss and SN ejecta has been more significant near the center than the outskirts.

We also detect emission from Si, S, Mg, and O and measure abundances for these elements. Determining the relative abundance of Fe and α-elements is critical for discriminating between the relative importance of Types II and Ia SNe in the parent galaxy (e.g., Renzini et al. 1993; Loewenstein et al. 1994). Therefore, these measurements provide important clues for our understanding of the evolution of both the stellar component and the hot ISM. If heavy elements are mainly synthesized in Type II SNe, the abundance ratio of α-elements to Fe is expected to be higher than the solar ratio (e.g., Woosley & Weaver 1995), while the ratio decreases with increasing contributions from Type Ia SNe (e.g., Iwamoto et al. 1999). In § 4.3 we show that the abundance ratio of Si to Fe is close to the solar ratio. Note that among α-elements, the abundance measurement of Si is least uncertain because of its strong, isolated emission features; the theoretical yields of Si are also the best determined, with the least amount of scatter between model predictions (e.g., Gibson et al. 1997; Nagataki & Sato 1998). With SN yields taken from Gibson et al. (1997) and converted to the revised solar values given by Grevesse & Sauval (1998), the measured abundance ratio of Si to Fe (near solar) indicates that 60%–80% of the detected iron mass is produced in Type Ia SNe.

S and Mg are found to be slightly less abundant (relative to Fe) than Si, but their abundance ratios are still consistent with the solar ratio within the statistical errors. O is the least abundant among the measured α-elements, appearing to have subsolar abundance ($\sim 3\ \sigma$) within the D_{25} ellipse of the galaxy (out to a radius of $\sim$40 kpc) and possibly increasing to the solar abundance ratio in the outskirts (at radii of 40–100 kpc). Because both Mg and O are mainly produced by Type II SNe, the apparent decrease of O/Mg at the center of NGC 507 is difficult to interpret with a simple combination of Types II and Ia SNe. Buote et al. (2003) reported a similar trend of low O abundance in the center of NGC 5044 (a galaxy similar to NGC 507 in both optical and X-ray properties) and suggested a warm absorber or an unknown physical/instrumental effect. Given the uncertainties discussed in § 4.3, we consider that the subsolar O abundance in the central regions of NGC 507 requires further confirmation.

While we see a significant radial variation in metal abundances in both Fe and α-elements, the ratio of Fe to α-element abundance appears to be constant, although a mild radial gradient, either positive or negative, may be allowed by the large error bars at large radii (see Fig. 5, *bottom right*). This constant ratio suggests that Types II and Ia SN ejecta are well mixed on a larger scale ($\sim$100 kpc) than the optical galaxy ($\sim$40 kpc), contrary to the conclusions based on the subsolar Fe abundances estimated with *ASCA* spectra (e.g., Mushotzky et al. 1996; Matsumoto et al. 1997). These results, which we believe were biased by the assumption of a simple emission model (see § 3), led to the suggestion of a considerably flatter IMF and less important Type Ia SN activity in elliptical galaxies (Loewenstein et al. 1994) than had been assumed on the basis of stellar evolution models for these systems (e.g., Renzini et al. 1993; Arimoto et al. 1997). Our results indicate that these constraints on the IMF and/or a reduced Type Ia SN rate are not needed.

5.2. *The Hot ISM (Temperature and Absorption)*

As discussed in § 3.2, the temperature of the hot ISM is not simply a function of the galactocentric radius. In addition to the overall temperature gradient detected in the *ROSAT* data (KF95), the hot ISM appears to consist (at each radius in a three-dimensional distribution) of at least two gaseous components with different temperatures. While the 1.4 keV component dominant at large radii may be representing the virialized hot halo, our result of a multiphase hot medium suggests that the central region of NGC 507 exhibits complex substructures, perhaps resulting from dynamical perturbations. These structures include two distinct emission peaks, possibly separated by the nuclear radio jet, seen in the high-resolution *Chandra* image (Forman et al. 2001; Paolillo et al. 2003). Also present are discontinuities of the X-ray surface brightness toward the northeast (Kraft et al. 2004) and the southwest (in a future paper). These features suggest either contact discontinuities or cold fronts, which could be indicative of recent mergers. In cosmological simulations of elliptical galaxies and clusters, a finite range of temperatures at a given radius is often found (e.g., Kawata & Gibson 2003). Therefore, it is clear that an overall radial temperature gradient alone does not reflect the real properties of the hot ISM.

As reported for other early-type galaxies and clusters (e.g., Peterson et al. 2001; Buote et al. 2003), we also find no thermal emission from gas cooler than $kT < 0.6$ keV (roughly half of the temperature in the ambient gas). Some heating mechanisms (such as AGN feedback or thermal conduction) could compensate the radiative cooling (e.g., Fabian 2003 and references therein). The lack of cooling below the observed limit is sometimes used to argue against a multitemperature model. However, this does not rule out temperatures in the observed range, between that in the ambient gas ($\sim$1.4 keV) and $\sim$0.6 keV.

The best-fit hydrogen column [$N_{\rm H} = (6$–$7) \times 10^{20}$ cm^{-2} in fit 8 of Table 1] is close to the Galactic line-of-sight value (5×10^{20} cm^{-2}). Our estimate is consistent with the *ROSAT* results (KF95) but considerably lower than the *ASCA* reports

of $N_{\rm H} = (1–2) \times 10^{21}$ cm^{-2}, which suggested absorption intrinsic to NGC 507 (Matsumoto et al. 1997; Matsushita et al. 2000). Neither *IRAS* far-IR (Knapp et al. 1989) nor H I observations (Knapp et al. 1985) of NGC 507, however, indicate significant internal absorption, yielding an upper limit of $M_{\rm H\,I}$ of 2.7×10^9 $M_\odot$. Since an intrinsic hydrogen column of a few times 10^{20} cm^{-2} within the D_{25} ellipse of NGC 507 would correspond to $M_{\rm H\,I} \sim 10^{10}$ $M_\odot$, we can rule out the presence of internal absorption in NGC 507, unless there is a significant amount of molecular gas (see Arabadjis & Bregman 1999). We note that $N_{\rm H}$ and the amount of hard component returned by the spectral fits are partially tied, in the sense that a larger $N_{\rm H}$ tends to go with a smaller hard component. This in turn would affect the model predictions for the thermal continuum at low ($E < 0.7$ keV) and high energies ($E > 2$ keV), reducing the required strength of the Fe peak at $\sim$1 keV. This effect could also be partly responsible for *ASCA* estimates of low abundances.

5.3. *The Hard Spectral Component*

How much X-ray emission do we expect from the LMXBs in NGC 507? Is this emission consistent with that inferred from our best-fit hard emission component? *Chandra* observations of giant elliptical galaxies have detected populations of discrete, pointlike sources, mostly LMXBs associated with the galaxies (e.g., $\sim$150 in NGC 1399; Angelini et al. 2001). Because of the distance to NGC 507, typical LMXBs cannot be detected in either our *XMM-Newton* observation or the existing 16 ks *Chandra* observation. In this *Chandra* image (ObsID 00317), only three nonnuclear sources can be barely detected within the D_{25} ellipse (Paolillo et al. 2003; also to be presented in a future paper). At a distance of 70 Mpc, typical LMXBs (with $L_{\rm X} = 10^{37}$–10^{38} ergs s^{-1}) in NGC 507 would result in less than 1 count in the above *Chandra* observation. Only ultraluminous X-ray sources (ULXs; with $L_{\rm X} > 10^{39}$ ergs s^{-1}) could possibly be detected. The total X-ray luminosity of an undetected LMXB can be determined indirectly by using its relationship with the optical luminosity. We use here the relationship determined by Kim & Fabbiano (2004) using a large sample of early-type galaxies observed with *Chandra*, for which these authors derived an incompleteness-corrected X-ray luminosity function within the D_{25} ellipse:

$$L_{\rm X}({\rm LMXB})/L_B = (0.9 \pm 0.5) \times 10^{30} \text{ ergs s}^{-1}\ L_{B,\odot}^{-1},$$

where $L_{\rm X}$ is measured in 0.3–8 keV and L_B is measured in units of $L_{B,\odot}$, adopting $M_{B,\odot} = 5.47$ mag. We estimate $L_{\rm X}({\rm LMXB}) = (1.2 \pm 0.7) \times 10^{41}$ ergs s^{-1} for $B_T^o = 12.19$ mag (taken from the Third Reference Catalog of Bright Galaxies), or $F_{\rm X}({\rm LMXB}) = (2.0 \pm 1.1) \times 10^{-13}$ ergs s^{-1} cm^{-2}, which is $\sim$2% of the total X-ray emission within 100 kpc, or $\sim$10% of $L_{\rm X}$ within D_{25} ($r < 40$ kpc). The flux of the hard component determined by our spectral fitting in this paper is in excellent agreement with the above estimate (Table 2). The best-fit normalization of the hard component (7 keV bremsstrahlung) inside $r < 2'$ (or 40 kpc) ranges between 2 and 3×10^{-13} ergs s^{-1} cm^{-2}.

As discussed in § 4.1, a nonnegligible amount (a few times 10^{-13} ergs s^{-1} cm^{-2}) of hard emission is found at radii outside the main stellar body of NGC 507 ($r = 60$–100 kpc), where we would not expect to find a significant amount of LMXBs. This external hard emission cannot be explained with background AGNs: based on the $\log N$–$\log S$ relationship determined in ChaMP (Kim et al. 2004), the expected X-ray flux of background sources within the annulus ($r = 60$–100 kpc) is about 10%–20% of the observed hard component. Another possibility is that this external hard emission may be related to the population of sources that we detect in the outer halo of NGC 507, in excess of the expected background sources (see Fig. 1). We will discuss these sources in a future paper.

6. CONCLUSIONS

We have presented the spatially resolved spectral analysis of the *XMM-Newton* observations of the halo-dominated X-ray emission of the elliptical galaxy NGC 507. After considering different effects in our spectral fitting, we conclude the following:

1. While the temperature of the hot ISM increases with increasing galactocentric radius as previously reported, the local ISM is not isothermal. Three-component emission models (two thermal gas components plus additional hard LMXB emission) are needed to model these data.
2. With these models, we find that the Fe abundance is supersolar (2–3 times solar) within the stellar body of NGC 507 (a radius of $\sim$40 kpc). The allowed maximum limit is $\sim$4 times solar. This is the highest $Z_{\rm Fe}$ reported for the hot ISM of an early-type galaxy, and it is fully consistent with the abundance predicted by the stellar evolution models. The Fe abundance decreases with galactocentric radius to values close to solar outside the optical galaxy, out to $r = 100$ kpc.
3. The α-element abundances (mainly determined by Si) are also supersolar, and the Fe–to–α-element abundance ratio is close to the solar ratio. The Fe-to-Si ratio suggests that 60%–80% of the Fe mass originates from Type Ia SNe.
4. While the Fe and α-element abundances decrease with increasing radius, their ratio remains solar out to 100 kpc. This, in addition to the near solar $Z_{\rm Fe}$ at large radii, indicates that Types II and Ia SN ejecta are well mixed throughout the hot ISM.
5. The hot ISM is likely in an inhomogeneous multiphase state with temperatures ranging from 0.6 to 1.4 keV (within a shell at a constant galactocentric distance). However, no cooling below 0.6 keV is identified. This is possibly related to the heating by the AGN, as indicated by the radio jet, or by thermal conduction.
6. Although we do not detect individual LMXBs in NGC 507, our spectral analysis indicates a hard component of $F_{\rm X} = (2–3) \times 10^{-13}$ ergs s^{-1} cm^{-2}, which is fully consistent with the expected amount, based on the $L_{\rm X}({\rm LMXB})$-L_B relation of early-type galaxies.

This work was supported by NASA grant NAG5-9965. We thank Nancy Brickhouse for useful discussions about emission codes and their uncertainties and the *XMM-Newton* User Support Team and Goddard Space Flight Center Guest Observer Facility for their help in data reduction.

REFERENCES

Anders, E., & Grevesse, N. 1989, Geochim. Cosmochim. Acta, 53, 197
Angelini, L., Loewenstein, M., & Mushotzky, R. F. 2001, ApJ, 557, L35
Arabadjis, J. S., & Bregman, J. N. 1999, ApJ, 510, 806
Arimoto, N., Matsushita, K., Ishimaru, Y., Ohashi, T., & Renzini, A. 1997, ApJ, 477, 128
Awaki, H., et al. 1994, PASJ, 46, L65
Buote, D. A. 2002, ApJ, 574, L135
Buote, D. A., & Fabian, A. C. 1998, MNRAS, 296, 977
Buote, D. A., Lewis, A. D., Brighenti, F., & Mathews, W. G. 2003, ApJ, 595, 151
Canizares, C. L., et al. 2000, ApJ, 539, L41
Davis, D. S., & White, R. E., III. 1996, ApJ, 470, L35
Ehle, M., et al. 2003, *XMM-Newton* Users' Handbook (Madrid: ESA), http://xmm.vilspa.esa.es/external/xmm_user_support/documentation/uhb_2.0
Fabbiano, G. 1995, in ASP Conf. Ser. 86, Fresh Views of Elliptical Galaxies, ed. A. Buzzoni, A. Renzini, & A. Serrano (San Francisco: ASP), 103
Fabbiano, G., Kim, D.-W., & Trinchieri, G. 1992, ApJS, 80, 531
Fabian, A. C. 2003, MNRAS, 344, L27
Forman, W., Markevitch, M., Jones, C., Vikhlinin, A., & Churazov, E. 2001, preprint (astro-ph/0110087)
Fukazawa, Y., Makishima, K., Tamura, T., Ezawa, H., Xu, H., Ikebe, Y., Kikuchi, K., & Ohashi, T. 1998, PASJ, 50, 187
Gastaldello, F., & Molendi, S. 2002, ApJ, 572, 160
Gibson, B. K., Loewenstein, M., & Mushotzky, R. F. 1997, MNRAS, 290, 623
Grevesse, N., & Sauval, A. J. 1998, Space Sci. Rev., 85, 161
Huchra, J. P., Vogeley, M. S., & Geller, M. J. 1999, ApJS, 121, 287
Irwin, J. A., Athey, A. E., & Bregman, J. N. 2003, ApJ, 587, 356
Iwamoto, K., Brachwitz, F., Nomoto, K., Kishimoto, N., Umeda, H., Hix, W. R., & Thielemann, F.-K. 1999, ApJS, 125, 439
Kawata, D., & Gibson, B. K. 2003, MNRAS, 346, 135
Kim, D.-W., & Fabbiano, G. 1995, ApJ, 441, 182 (KF95)
———. 2003, ApJ, 586, 826
———. 2004, ApJ, 611, 846
Kim, D.-W., Fabbiano, G., Matsumoto, H., Koyama, K., & Trinchieri, G. 1996, ApJ, 468, 175
Kim, D.-W., et al. 2004, ApJ, 600, 59
Knapp, G. R., Guhathakurta, P., Kim, D.-W., & Jura, M. 1989, ApJS, 70, 329
Knapp, G. R., Turner, E. L., & Cunnifee, P. E. 1985, AJ, 90, 454
Kraft, R. P., Forman, W. R., Churazov, E., Laslo, N., Jones, C., Markevitch, M., Murray, S. S., & Vikhlinin, A. 2004, ApJ, 601, 221
Loewenstein, M., Mushotzky, R. F., Tamura, T., Ikebe, Y., Makishima, K., Matsushita, K., Awaki, H., & Serlemitsos, P. J. 1994, ApJ, 436, L75
Lumb, D. H., Warwick, R. S., Page, M., & De Luca, A. 2002, A&A, 389, 93
Matsumoto, H., Koyama, K., Awaki, H., Tsuru, T., Loewenstein, M., & Matsushita, K. 1997, ApJ, 482, 133
Matsushita, K., Ohashi, T., & Makishima, K. 2000, PASJ, 52, 685
Matsushita, K., et al. 1994, ApJ, 436, L41
Mushotzky, R., Loewenstein, M., Arnaud, K. A., Tamura, T., Fukazawa, Y., Matsushita, K., Kikuchi, K., & Hatsukade, I. 1996, ApJ, 466, 686
Nagataki, S., & Sato, K. 1998, ApJ, 504, 629
O'Sullivan, E., & Ponman, T. J. 2004, MNRAS, 349, 535
O'Sullivan, E., Vrtilek, J. M., Read, A. M., & David, L. P. 2003, MNRAS, 346, 525
Paolillo, M., Fabbiano, G., Peres, G., & Kim, D.-W. 2003, ApJ, 586, 850
Peterson, J. R., Kahn, S. M., Paerels, F. B. S., Kaastra, J. S., Tamura, T., Bleeker, J. A. M., Ferrigno, C., & Jernigan, J. G. 2003, ApJ, 590, 207
Peterson, J. R., et al. 2001, A&A, 365, L104
Renzini, A., Ciotti, L., D'Ercole, A., & Pellegrini, S. 1993, ApJ, 419, 52
Snowden, S., Still, M., Harrus, I., Arida, M., & Perry, B. 2002, An Introduction to *XMM-Newton* Data Analysis, Ver. 1.3, http://heasarc.gsfc.nasa.gov/docs/xmm/abc/abc.html
Trinchieri, G., Fabbiano, G., & Kim, D.-W. 1997, A&A, 318, 361
Trinchieri, G., Kim, D.-W., Fabbiano, G., & Canizares, C. R. 1994, ApJ, 428, 555
Woosley, S. E., & Weaver, T. A. 1995, ApJS, 101, 181
Xu, H., et al. 2002, ApJ, 579, 600